nature physics

ARTICLES

https://doi.org/10.1038/s41567-019-0600-y

Topological chaos in active nematics

Amanda J. Tan[1], Eric Roberts[2], Spencer A. Smith[3], Ulyses Alvarado Olvera[1], Jorge Arteaga[1], Sam Fortini[1], Kevin A. Mitchell[1*] and Linda S. Hirst[1*]

Active nematics are out-of-equilibrium fluids composed of rod-like subunits, which can generate large-scale, self-driven flows. We examine a microtubule-kinesin-based active nematic confined to two dimensions, exhibiting chaotic flows with moving topological defects. Applying tools from chaos theory, we investigate self-driven advection and mixing on different length scales. Local fluid stretching is quantified by the Lyapunov exponent. Global mixing is quantified by the topological entropy, calculated from both defect braiding and curve extension rates. We find excellent agreement between these independent measures of chaos, demonstrating that the extensile stretching between microtubules directly translates into macroscopic braiding of positive defects. Remarkably, increasing extensile activity (through ATP concentration) does not increase the dimensionless topological entropy. This study represents an application of chaotic advection to the emerging field of active nematics and quantification of the collective motion of an ensemble of defects (through topological entropy) in a liquid crystal.

Nature provides many examples of active matter, ranging from flocks of birds[1], fish[2] and insects[3] to sheets of cells[4–6] and swarms of bacteria[7–9]. In the laboratory, various attempts have been made to develop biomimetic and synthetic active materials, from self-propelled colloids[10,11] and mechanically agitated flocks[12] to dense phases of biopolymers driven by molecular motors[13–23]. This is a rich field of research, and so far much theoretical work has been dedicated to understanding the fundamental physics of these fascinating and diverse systems[24,25]. Active materials are non-equilibrium systems, and thus they cannot be described in the framework of conventional thermodynamics. The unifying theme of active matter is that collections of subunits consume energy locally, translate this energy into movement and ultimately produce large-scale flows. This large-scale motion can produce rich emergent structures, including phase boundaries and topological defects, where local order breaks down.

The central theme of this work is the introduction of concepts from chaotic advection[26,27] to the physics of biologically active fluids. These concepts include topological entropy and Lyapunov exponents, which are well known measures of chaos in the theory of chaotic advection but have been thus far largely overlooked in studies of active matter. Roughly speaking, the Lyapunov exponent measures the rate at which nearby fluid parcels separate from one another. The topological entropy, on the other hand, measures the asymptotic (in time) exponential growth rate in the length of a material curve as it is stretched within the fluid. We use spatially (and temporally) averaged local measurements in the fluid to estimate the Lyapunov exponent. To estimate the topological entropy, we use larger-scale measurements, including the global braiding motion of topological defects about one another.

In experimental studies of chaotic advection in passive fluids at low Reynolds number[28], fluid motion is often driven at the boundary, either by tangentially sliding the boundary, for example rotating a cylindrical boundary wall[29–31], or by directly stirring the fluid with inserted rods[28,32–34]. The resulting chaotic flow produces exponentially stretching material curves. In stirring experiments, chaos is observed when three or more rods are inserted into the fluid and moved around one another in a braiding motion[28,32–34]. The mathematical braid can be visualized by interpreting time as the vertical dimension. Figure 1a shows an example braid, with the initial effect of this braid on a line of dye shown schematically in Fig. 1b. Repeated applications of this stirring pattern generate an experimental image such as Fig. 1c, taken from ref. [28]. The overall mixing efficiency depends on the stirring pattern, particularly on the topological braid type of the motion, and can be quantified by the topological entropy, that is the growth rate of material lines as fluid elements are stretched apart from each other. One remarkable mathematical fact is that a given braid type of the rod motion guarantees a specific minimal amount of topological entropy in the dynamics; for example, the Fig. 1a braid generates an entropy of $\log[(1+\sqrt{5})/2] = 0.4812$ for each swap of two strands. In fact, any collection of passively advected orbits in the fluid, not just those next to the stirring rods, generates a braid type, with an associated minimal topological entropy; such trajectories have been described as 'ghost rods' in the literature[33,34]. Though the mathematics is more rigorous when such trajectories are periodic in time, recent work has generalized the analysis to open, aperiodic trajectories[35–38].

Our experiments use an extensile-active-nematic fluid confined to a quasi-two-dimensional (2D) layer[15,16,18] (Fig. 1d). The fluid consists of purified microtubules and kinesin-1 molecular motor proteins (Fig. 2a and Preparation of the 2D active nematic). In biological cells, these molecules exist in the cytoskeleton, where the microtubules form highways for the motors. The motor proteins step stochastically along a microtubule in a net direction defined by the microtubule's structural polarity, a process that consumes energy from the hydrolysis of ATP. This force-generating action is essential for a variety of cell functions, including organelle transport[39], cell division and cytoplasmic streaming[40].

In our laboratory set-up, microtubules condense into bundles, cross-linked by clusters of streptavidin-bound kinesin motors (Fig. 2a and Methods). If two motors in a cluster bind to adjacent microtubules of opposite polarities, the opposing forces produce a sliding motion between these microtubules. Thus neighbouring bundles of opposing polarities extend away from each other to generate local fluid stretching. Under the dense confinement of a 2D oil–water interface, the bundles enter the nematic phase, with a well defined director field recording the local bundle orientation (Figs. 1d and 2b). In the presence of ATP, the bundles continually move, extend,

[1]Physics Department, University of California, Merced, CA, USA. [2]Applied Math Department, University of California, Merced, CA, USA. [3]Department of Physics, Mount Holyoke College, South Hadley, MA, USA. *e-mail: kmitchell@ucmerced.edu; lhirst@ucmerced.edu

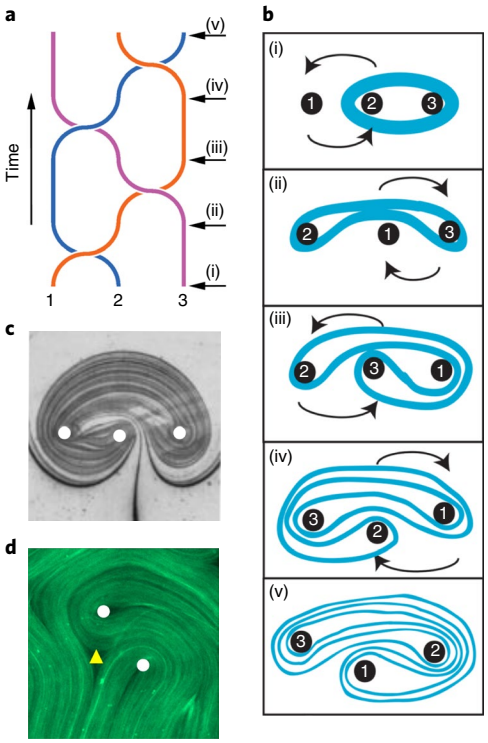

Fig. 1 | Topological stirring of fluids. a, Braid diagram representing three rods as they stir a 2D fluid in a pattern known as the golden braid. Time moves up in the vertical direction. Each strand represents the world line of one rod. The times denoted (i)–(v) correspond to the schematic in **b**. **b**, The impact of passive stirring generated by the braid in **a** on an initial line of dye. As the rods sequentially exchange positions, the dye stretches. **c**, Experimental image of lines of dye stirred by three rods after several iterations of rod exchanges according to the stirring protocol shown in **a**. The rod positions are highlighted in white. **d**, Fluorescence microscopy image of the active nematic fluid with topological defects marked. White circles denote +1/2 defects; a yellow triangle denotes a −1/2 defect. Panel **c** adapted from ref. [28], Cambridge Univ. Press.

bend, buckle and break[15,16,18]. This continual motion advects individual tubulin monomers throughout the fluid in a chaotic fashion (Supplementary Video 1). As a result, pairs of +1/2 and −1/2 topological defects (Fig. 1d) in the director field are continuously created and annihilated. Between their birth and death, topological defects move around one another in a complicated braiding pattern, as shown in Fig. 3. (See also Supplementary Video 2.)

The pattern of microtubule bundles surrounding the +1/2 defects (Fig. 1d) strongly resembles the pattern of dye surrounding stirring rods (Fig. 1c) in passive advection. The active nematic fluid described here differs crucially from a conventional passive fluid in that internal flows and chaotic advection in a passive fluid must be driven externally. In this report, we show that braiding by topological defects in the active fluid produces macroscopic chaotic advection, and thus the defects act as virtual stirring rods. In addition, we demonstrate that mixing on the macroscale by virtual rods arises spontaneously as a consequence of the molecular-level sliding action. This relationship is quantified by the topological entropy and Lyapunov exponent.

One consequence of topological mixing theory is that exponential stretching cannot exist within the fluid without some non-trivial braiding of defects, as quantified by the topological entropy. It is particularly interesting that this self-driven fluid spontaneously creates a set of defects that must then move in a particular way to produce exactly the topological entropy needed to accommodate the local stretching. This observation sheds new light on previous studies of defect dynamics. For example, in the numerical work of Shendruk et al.[22], the authors demonstrated a particular braiding pattern resembling a ceilidh dance, in which defects braid around one another in two counter-propagating lines in a channel. In fact, this particular braid has been studied in the chaotic advection literature, where it is known as the 'silver braid'[34]; interestingly, it has been proved to be optimal, in that it provides the largest amount of topological entropy per time step for any linear arrangement of defects. Thus, if one were to compute the stretching rate for this flow a priori, one could reasonably conjecture that the ceilidh dance pattern was topologically mandated to accommodate all the topological entropy.

We measure both the topological entropy and the Lyapunov exponent of the active flow; we measure the topological entropy using three distinct methods, designed to probe the system across different length scales. The Lyapunov exponent is obtained from the velocity-gradient tensor field, itself computed from particle image velocimetry (PIV) using fluorescence microscopy images of the microtubule bundles. The topological entropy is measured directly using beads attached to the microtubules. As two beads pass and separate after a close approach, the exponential growth rate of the nematic contour connecting them is measured. Alternatively, the same measurement is made using the separation of neighbouring topological defects. The third independent measurement of the topological entropy derives from the braiding motion of the topological defects about one another. We find that the positive topological defects act as virtual stirring rods, generating all of the topological entropy from their braiding motion; negative topological defects add very little, if any, additional entropy. The three measures of topological entropy are consistent with one another, which is remarkable given that braiding is a manifestly global and topological technique, independent of geometric details, whereas the stretching techniques depend inherently on length measurements. Furthermore, the topological entropy is slightly larger than the Lyapunov exponent, reflecting a fundamental theorem in 2D chaotic dynamics[41]. Measurements are repeated at progressively higher ATP concentrations. Increasing the ATP concentration raises the system activity, increasing the overall fluid speed. The Lyapunov exponent and topological entropy generally also increase with increasing fluid speed. We non-dimensionalize these quantities to isolate the purely topological effects on mixing efficiency when we increase system activity. Across all methods we obtain a fascinating result: the dimensionless Lyapunov exponent and dimensionless topological entropy are constant with ATP concentration. This result suggests that these dimensionless quantities may be universal features of the fully developed 'turbulent' state of the active nematic.

Topological entropy from bead and defect separations

We first describe the measurement of separation rate in the nematic contour joining two beads. Biotin-coated silica beads of 2 μm diameter were bound to the microtubule bundles through free binding sites on the streptavidin molecules that form the kinesin clusters (Fig. 2a and Methods). This approach differs fundamentally from recent work on a similar system in which beads were passivated to avoid microtubule attachment, thus acting as passive tracers for the surrounding aqueous flow[15,16]. In contrast, bound beads track the microtubule network itself. The beads move within the nematic plane, where they are imaged with bright-field optical microscopy (Fig. 2c and Supplementary Video 3). Bead trajectories directly map the motion of microtubule segments throughout the system, including through bundle fracture and annealing.

After bead trajectories were extracted from a bright-field microscopy video, they were searched for close approaches of bead pairs (within 2–10 μm of each other). Following a close approach,

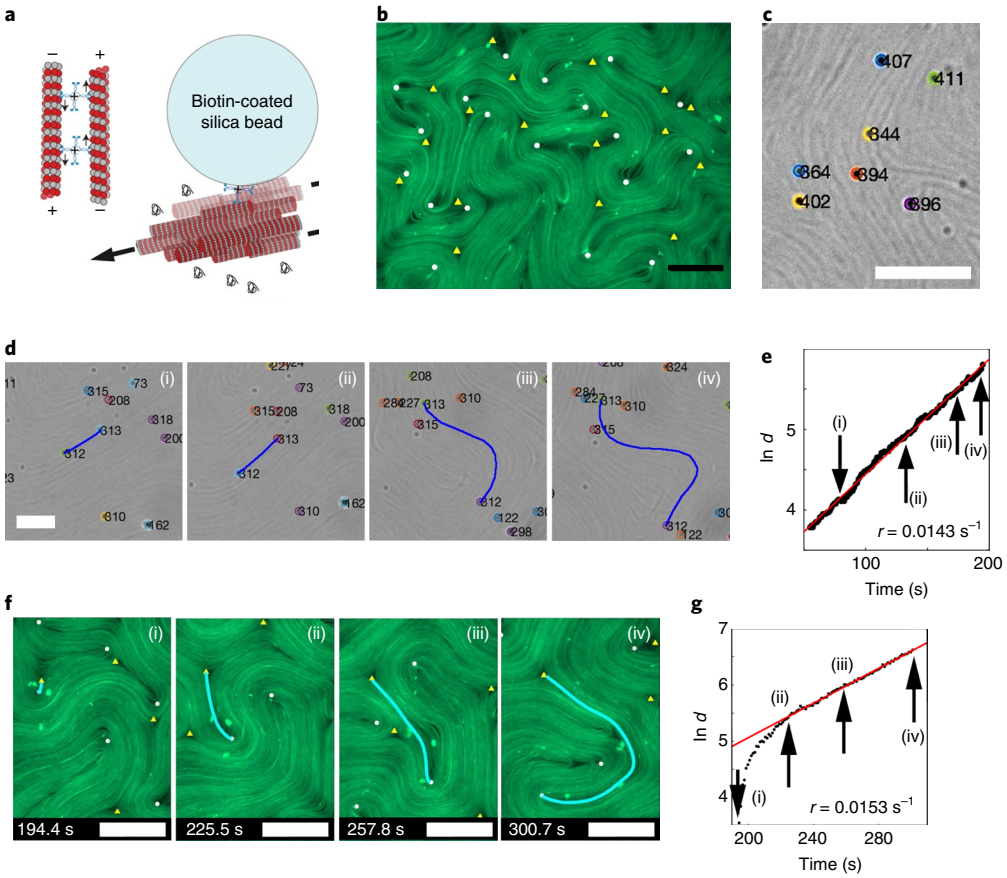

Fig. 2 | Measurement of separation rates in the active fluid. a, Schematic showing elements of the microtubule network, consisting of microtubules cross-linked by kinesin clusters. The microtubule bundles of opposite polarities extend away from each other as the kinesin motors walk. Biotin-coated silica beads are used to bind onto free streptavidin-binding sites in kinesin clusters to attach onto the microtubule network. **b**, Fluorescence microscopy image of microtubule network in two dimensions at an oil–water interface with marked topological defects. White circles are +1/2 defects and yellow triangles are −1/2 defects. Scale bar, 100 μm. **c**, Bright-field microscopy image of beads attached to the microtubule network. Beads are numbered automatically for tracking. Scale bar, 50 μm. **d**, Bright-field microscopy time lapse showing contour length growth between two beads moving away from each other at 50 μM ATP concentration. Scale bar, 30 μm. **e**, Semi-log plot of contour length, d (μm), as a function of time for the bead pair shown in **d** with times (i)–(iv) marked by arrows. We make a linear fit with slope r. **f**, Time-lapse fluorescence microscopy images tracking the separation of a +1/2 defect (white) and −1/2 defect (yellow), shown by the cyan curve. Scale bars, 100 μm. **g**, Semi-log plot of defect separation distance d (μm) as a function of time for a defect pair. A linear fit with slope r was made after the transient rise. The marked times (i)–(iv) correspond to the images in **f**.

the pair of beads moves apart, with a nematic contour, that is an integral curve of the nematic director field, stretching between them. Physically, the nematic contour represents the microtubule bundles connecting the beads; it grows and bends with the fluid as the bundles extend. For each image frame, the nematic contour was manually traced (Fig. 2d and Supplementary Video 4). The slope of the natural log of the separation contour length versus time yields the separation rate r (Fig. 2e). The result shows clear exponential growth over nearly an order of magnitude in contour length. A total of nine pairs of beads were analysed (Supplementary Fig. 1). r is remarkably similar across bead pairs, with mean $\langle r\rangle = 0.0143\,\mathrm{s}^{-1}$ and s.d. $\sigma = 0.0016\,\mathrm{s}^{-1}$ (Supplementary Fig. 2). To estimate the topological entropy, we perform a weighted average as discussed in Supplementary Section 1, resulting in $h_{\mathrm{bead}} = 0.0145\ (\pm 0.0001)\,\mathrm{s}^{-1}$.

In a second approach, we measured the separation rate between topological defects, instead of beads. Pairs of nearby +1/2 and −1/2 defects were identified in fluorescence microscopy videos. Fluorescence microscopy enhances the microtubule structure while eliminating the non-fluorescent beads (Supplementary Video 1). We then identified the nematic contour between the defects as a function of time (Fig. 2f) (Supplementary Section 2). This contour length increased exponentially (Fig. 2g), yielding the exponential r. A total of 10 defect pairs were analysed, resulting in $h_{\mathrm{defect}} = 0.0142\ (\pm 0.0002)\,\mathrm{s}^{-1}$ (Supplementary Fig. 3). Results from defect and bead separations are remarkably consistent, implying that the separation rate between defects is a good proxy for the growth of material curves anywhere in the fluid.

Topological entropy from defect braiding

Whereas the first two computations of topological entropy used the growth in Euclidean contour length, our third approach is purely topological and independent of the first two. This approach views the topological defects as stirring rods, and computes the topological entropy by the braiding pattern of these rods around one another (Fig. 3a). As such, the method is insensitive to the exact positions of the defects. However, the original defect trajectories must be extended to exist for all times, as described in Supplementary Section 3.

We use the recently developed E-tec algorithm[38] to extract topological entropy from defect trajectories. This algorithm uses a computational geometry approach to propagate an initial piecewise linear elastic mesh (Fig. 3b) forward in time. As trajectories evolve,

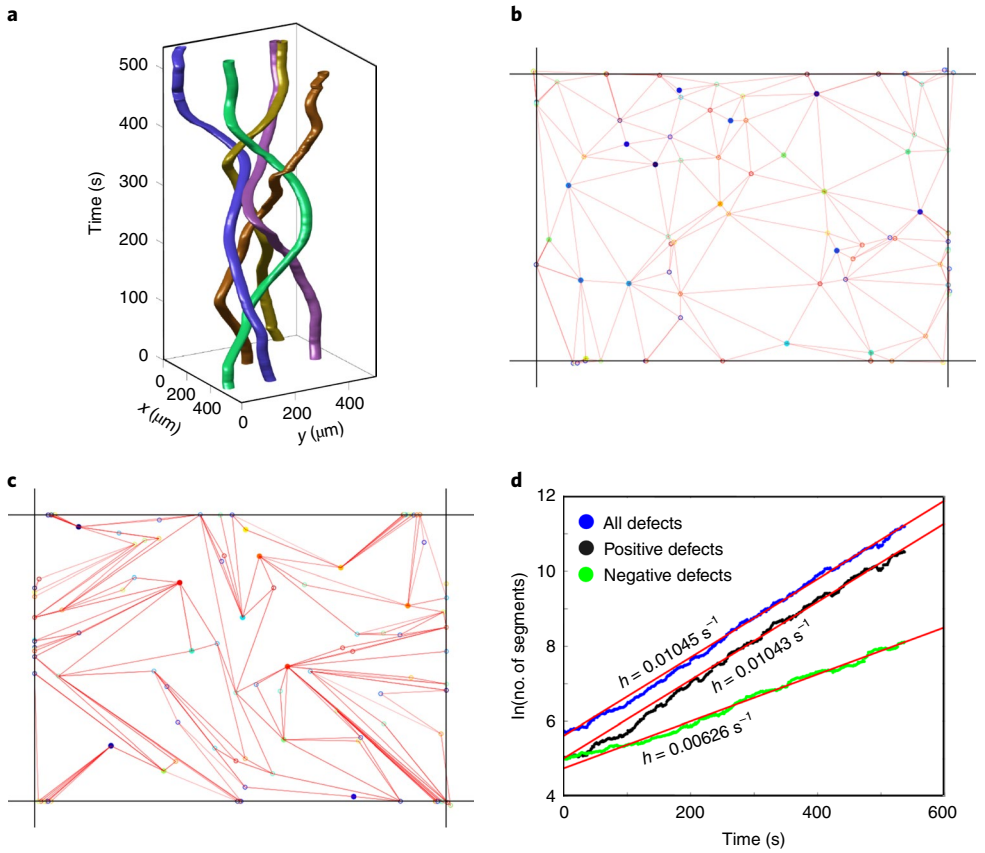

Fig. 3 | E-tec computation of topological entropy. a, A sampling of positive defect trajectories braiding around one another. **b**, Initial mesh between defects inside the black bounding box. Filled circles are actual defects. Open circles are 'extinct' defect trajectories, as discussed in Supplementary Material. **c**, Final stretched mesh and defect positions. The intensities of the red segments indicate their weights. **d**, Plot showing topological entropy, h, calculated using the E-tec algorithm for positive defects only, 0.01043 (±0.00080) s^{-1}, negative defects only, 0.00626 (±0.00032) s^{-1}, and all defects, 0.01045 (±0.00053) s^{-1}. Errors on the E-tec growth rates were computed as the difference in the slopes fitted over two distinct time intervals: interval 215–537 s and interval 322–537 s.

the mesh is stretched and folded over itself, creating an exponentially growing number of line segments. Figure 3c shows the final stretched mesh and Fig. 3d shows the growth in the number of segments as the fluid is 'stirred' by the defects. The exponential growth rate is the topological entropy generated by the stirring rods, which in general is only a lower bound to the true topological entropy of the fluid. In Navier–Stokes simulations of stirring a 2D fluid, there can be significantly more entropy than predicted by the motion of the rods.

In principle, any ensemble of trajectories passively advected in the fluid can be viewed as virtual stirring rods, and the corresponding topological entropy computed using E-tec. Again, such ensembles typically provide only a lower bound on the true entropy of the flow—the greater the number of trajectories included, the greater the lower bound. In some special cases, a small number of specifically chosen trajectories generate all of the topological entropy[38].

Figure 3d shows three results, corresponding to stirring by just the +1/2 defects, by just the −1/2 defects and by both +1/2 and −1/2 defects. The entropy from the +1/2 defects, 0.01043 (±0.00080) s^{-1}, is significantly larger than that of the −1/2 defects, 0.00626 (±0.00032) s^{-1}. Most remarkable, however, is that the entropy from all the defects, 0.01045 (±0.00053) s^{-1}, is essentially the same as from just the positive defects. The negative defects introduce no additional stretching. This is a surprisingly strong result, and shows that the positive defects are the special points for generating topological mixing and that they alone can account for all the topological entropy in the fluid.

Finally, the E-tec computation must be corrected for the finite size of the image domain. This correction is estimated by the escape rate of trajectories (Supplementary Section 4), which is computed from the bead data to be 0.00291 (±0.00003) s^{-1}. Adding this to the E-tec result yields a final entropy $h_{braid} = 0.0133$ (±0.0008) s^{-1}.

The fact that the separation-rate and braiding methods agree so well is by no means trivial or expected. Several assumptions are needed to justify why either of these methods should yield the true topological entropy (Supplementary Sections 1 and 4). Such assumptions are only verified through an analysis of the experimental data. Thus, the agreement of these two measures is a significant experimental finding. For example, solid-state topologically ordered systems may have defect translation without any stretching or motion of the underlying material. In the microtubule active nematic system, the strong coupling between motion of the microtubules themselves and motion of the defects is necessary to see the agreement reported here. (This coupling only breaks down near the creation and annihilation of defect pairs; Supplementary Fig. 1e,f.)

Finally, we computed the Lyapunov exponent directly from the microtubule velocity field as $\lambda_{\nabla v} = 0.0120$ (±0.0006) s^{-1} (Lyapunov exponent from velocity field). Figure 4 shows all four measures of chaos at 50 μM ATP concentration. The Lyapunov exponent is slightly less than the three measurements of topological entropy. This is consistent with a general result from dynamical systems theory, which states that the topological entropy is always greater than or equal to the metric entropy (also known as the measure-theoretic

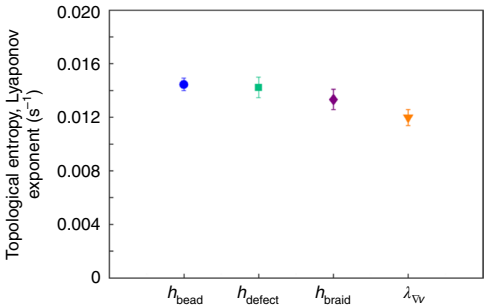

Fig. 4 | Comparison of the four measures of chaos at 50 μM ATP concentration. The error bars for h_{bead} and h_{defect} are the s.e.m., when averaging over the set of separation rates. The error on h_{braid} is essentially just that of the fit described in Fig. 3. The error on $\lambda_{\nabla}\mathbf{v}$ is based on the error of the PIV analysis, estimated at 5%. See Supplementary Section 5.

or Kolomogorov–Sinai entropy)[41]. In 2D area-preserving flows, the metric entropy is equal to the positive Lyapunov exponent, implying the relative ordering seen in Fig. 4. The fact that the Lyapunov exponent is only slightly less than the topological entropy reflects the statistical homogeneity of the active nematic flow. If the local Lyapunov exponent were constant in space and time, the topological entropy would be exactly equal to the Lyapunov exponent.

Variation of ATP concentration

To investigate the effects of increasing activity on chaotic advection, we ran a series of experiments at different ATP concentrations (50–1,000 μM). Because ATP concentration controls the kinesin step-rate at the molecular level, we expect the topological entropy and Lyapunov exponent to increase with increasing ATP concentration.

When single microtubules glide on a kinesin-decorated glass surface, their gliding velocity as a function of ATP concentration is generally well described on a local level by Michaelis–Menten kinetics[42–44]. Similarly, we observed that the average root-mean-squared velocity v_{rms} (see 'PIV analysis') for our attached beads also follows Michaelis–Menten kinetics under ATP variation (Fig. 5a).

Henkin et al. used passive unattached tracers to measure the average bead speed in a similar, three-dimensional microtubule network as a function of ATP concentration (0.5–3 mM)[16]; they observed a monotonic increase to 2 μm s^{-1} at saturation. Our attached-bead method, however, contains richer and more direct information on the motion of the microtubules themselves.

We calculated topological entropy h_{bead} for bead pairs at different ATP concentrations (50–1,000 μM) (Fig. 5b). Separation rates were measured for about 10 bead pairs at each concentration. (See raw data in Supplementary Fig. 2.) Though Fig. 5b shows a general upward trend, it is not strictly monotonic. For context, we consider the relevant physical scales. An inverse-time scale τ^{-1} for h_{bead} can be obtained by combining the characteristic velocity v_{rms} with a characteristic length ℓ. Following refs. [23,45], we chose ℓ to be the length at which the velocity–velocity correlation function, computed from PIV velocities, decays to half its maximum value (Fig. 5c) (PIV velocity analysis). ℓ varies only modestly with ATP concentration, consistent with the work of Lemma et al.[23] for ATP concentrations larger than 10 μM. References [23,45] establish that ℓ arises from balancing the elastic bend energy of the microtubule bundles with motor activity. Thus, if only the activity were increased, ℓ should decrease, and indeed, except for the 250 μM data, our results are consistent with a small downward trend. The outlier at 250 μM ATP concentration could be understood in terms of a slight change in the microtubule lengths, which would affect the correlation length. Microtubule bundle length is very sensitive to sample preparation, such as pipette shearing.

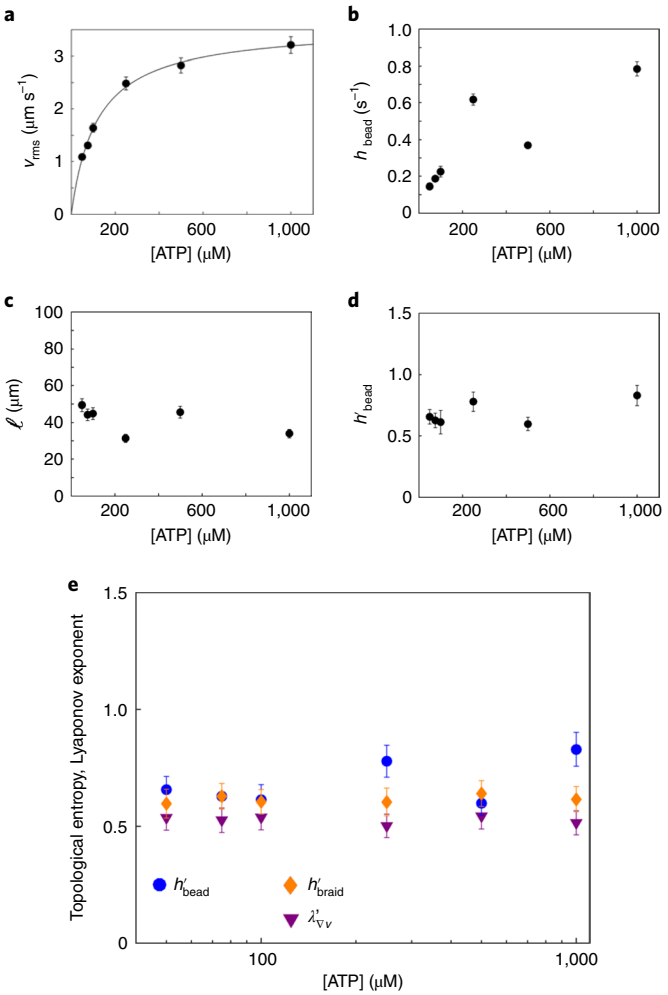

Fig. 5 | Non-dimensionalized topological entropy and Lyapunov exponent are insensitive to motor activity. a, Average v_{rms} of beads as a function of ATP concentration. This relationship follows Michaelis–Menten kinetics (solid curve), $v = (v_{max}[ATP])/([ATP] + K_m)$, with fit parameters $K_m = 120$ (±20) μM and $v_{max} = 3.57$ (±0.19) μm s^{-1}. **b**, Topological entropy computed from bead separation as a function of ATP concentration. **c**, ℓ as a function of ATP concentration. **d**, Dimensionless topological entropy h'_{bead} versus ATP concentration. This was obtained by multiplying the original entropy h'_{bead} in **b** by the characteristic time derived from **a** and **c**. **e**, All four dimensionless measures of chaos as a function of ATP concentration. Error bars on the dimensionless measures include the errors on the characteristic length and velocity, which combine to give an error on the timescale $\Delta\tau = \tau[(\Delta\ell/\ell)^2 + (\Delta v_{rms}/v_{rms})^2]^{1/2}$. The error on h'_{bead}, for example, is then $\Delta h'_{bead} = h'_{bead}[(\Delta h_{bead}/h_{bead})^2 + (\Delta\tau/\tau)^2]^{1/2}$.

We obtain the dimensionless topological entropy $h'_{bead} = \tau h_{bead}$ by rescaling by the characteristic time $\tau = \ell/v_{rms}$ (Fig. 5d). This scales out any fluctuations in either ℓ or v_{rms} due to experimental factors, resulting in a measure of topological entropy that depends only on the flow geometry. Surprisingly, the dimensionless entropy h'_{bead} is nearly constant with ATP concentration; although the system moves faster with increased ATP, the underlying geometric complexity of the mixing remains constant. This suggests that the dimensionless topological entropy may be a universal quantity for the fully turbulent state of active nematics.

For each ATP concentration, we also computed the other measures of chaos. The two separation-based entropies are in close agreement (Supplementary Fig. 5). Figure 5e thus shows just the

bead-separation entropy compared with the other two measures. Again, each dimensionless measure varies little with ATP. The average of the bead entropy is $\langle h'_{\mathrm{bead}}\rangle = 0.684$, with braiding entropy somewhat lower at $\langle h'_{\mathrm{braid}}\rangle = 0.614$. As expected, the Lyapunov exponent, $\langle \lambda'_{\nabla v}\rangle = 0.526$, is below all measures of topological entropy. There are two main reasons why $\langle h'_{\mathrm{braid}}\rangle$ may be lower than $\langle h'_{\mathrm{bead}}\rangle$. First, the estimate of the finite-size effect of the image domain may fail to account for the full complexity of braiding near the boundary. Second, the extinct defects that exist before and after defect creation and annihilation events are passively advected by the PIV velocity field, which has some error in the velocity component along the director.

Active fluids have emerged as an exciting frontier in soft-matter physics, but until now their flows have not been examined in detailed experiments from the perspective of chaotic dynamics. Using this approach, we have investigated the spontaneous 'self-mixing' of an extensile active nematic.

It is well appreciated that energy injected by molecular motors into active nematics at the molecular scale produces large-scale flows. Our results support the complementary view that fluid stretching is also injected into the flow of an active nematic at the molecular scale. This stretching can be quantified by the Lyapunov exponent. The fluid flow must respond on the macroscale in a manner consistent with this local stretching. Consistency requires that the +1/2 defects, which drive the stirring, braid around one another in a manner sufficiently complex to produce topological entropy greater than the Lyapunov exponent. The number, density and speed of the defects are not sufficient, in themselves, to produce topological entropy. The braiding pattern is critical. Our data demonstrate that the topological entropy of the moving defects is greater than the stretching injected through kinesin-motor-driven filament sliding; the excess entropy, that is the difference between topological entropy and the Lyapunov exponent, is shown to be quite small, reflecting the homogeneity of the fluid motion.

In total, four different chaotic mixing measurements are taken across a range of activity levels (tuned through ATP concentration) to calculate the topological entropy and Lyapunov exponents. The results are consistent across all four techniques. Remarkably, when non-dimensionalized, these quantities do not depend significantly on ATP concentration. This suggests that the dimensionless topological entropy and/or Lyapunov exponent of this system may be a universal feature of the turbulent state of such systems. It would be interesting to probe this hypothesis by varying other parameters, such as kinesin density or oil viscosity. It would also be interesting to probe the topological entropy as the system evolves across the transition from the non-turbulent to the fully turbulent state. For example, is the rise in topological entropy sharp or gradual?

Finally, we propose that this microtubule–kinesin system can be considered as a chemically driven self-mixing fluid, opening the door for a potential new class of non-equilibrium energy-dissipative solvents.

Online content

Any methods, additional references, Nature Research reporting summaries, source data, statements of code and data availability and associated accession codes are available at https://doi.org/10.1038/s41567-019-0600-y.

Received: 29 January 2019; Accepted: 19 June 2019;
Published online: 5 August 2019

References

1. Toner, J. & Tu, Y. Long-range order in a two-dimensional dynamical XY model: how birds fly together. *Phys. Rev. Lett.* **75**, 4326–4329 (1995).
2. Katz, Y., Tunstrøm, K., Ioannou, C. C., Huepe, C. & Couzin, I. D. Inferring the structure and dynamics of interactions in schooling fish. *Proc. Natl Acad. Sci. USA* **108**, 18720–18725 (2011).
3. Buhl, J. et al. From disorder to order in marching locusts. *Science* **312**, 1402–1406 (2006).
4. Saw, T. B. et al. Topological defects in epithelia govern cell death and extrusion. *Nature* **544**, 212–216 (2017).
5. Kawaguchi, K., Kageyama, R. & Sano, M. Topological defects control collective dynamics in neural progenitor cell cultures. *Nature* **545**, 327–331 (2017).
6. Prost, J., Jülicher, F. & Joanny, J.-F. Active gel physics. *Nat. Phys.* **11**, 111–117 (2015).
7. Sokolov, A., Aranson, I. S., Kessler, J. O. & Goldstein, R. E. Concentration dependence of the collective dynamics of swimming bacteria. *Phys. Rev. Lett.* **98**, 158102 (2007).
8. Wensink, H. H. et al. Meso-scale turbulence in living fluids. *Proc. Natl Acad. Sci. USA* **109**, 14308–14313 (2012).
9. Dunkel, J. et al. Fluid dynamics of bacterial turbulence. *Phys. Rev. Lett.* **110**, 228102 (2013).
10. Palacci, J., Sacanna, S., Steinberg, A. P., Pine, D. J. & Chaikin, P. M. Living crystals of light-activated colloidal surfers. *Science* **339**, 936–940 (2013).
11. Yan, J. et al. Reconfiguring active particles by electrostatic imbalance. *Nat. Mater.* **15**, 1095–1099 (2016).
12. Narayan, V., Menon, N. & Ramaswamy, S. Nonequilibrium steady states in a vibrated-rod monolayer: tetratic, nematic, and smectic correlations. *J. Stat. Mech. Theory Exp.* **2006**, P01005 (2006).
13. Ndlec, F. J., Surrey, T., Maggs, A. C. & Leibler, S. Self-organization of microtubules and motors. *Nature* **389**, 305–308 (1997).
14. Schaller, V., Weber, C., Semmrich, C., Frey, E. & Bausch, A. R. Polar patterns of driven filaments. *Nature* **467**, 73–77 (2010).
15. Sanchez, T., Chen, D. T. N., DeCamp, S. J., Heymann, M. & Dogic, Z. Spontaneous motion in hierarchically assembled active matter. *Nature* **491**, 431–434 (2012).
16. Henkin, G., DeCamp, S. J., Chen, D. T. N., Sanchez, T. & Dogic, Z. Tunable dynamics of microtubule-based active isotropic gels. *Phil. Trans. R. Soc. Lond. A* **372**, 20140142 (2014).
17. Giomi, L. Geometry and topology of turbulence in active nematics. *Phys. Rev. X* **5**, 031003 (2015).
18. DeCamp, S. J., Redner, G. S., Baskaran, A., Hagan, M. F. & Dogic, Z. Orientational order of motile defects in active nematics. *Nat. Mater.* **14**, 1110–1115 (2015).
19. Guillamat, P., Ignés-Mullol, J. & Sagués, F. Control of active liquid crystals with a magnetic field. *Proc. Natl Acad. Sci. USA* **113**, 5498–5502 (2016).
20. Doostmohammadi, A., Shendruk, T. N., Thijssen, K. & Yeomans, J. M. Onset of meso-scale turbulence in active nematics. *Nat. Commun.* **8**, 15326 (2017).
21. Guillamat, P., Ignés-Mullol, J. & Sagués, F. Taming active turbulence with patterned soft interfaces. *Nat. Commun.* **8**, 564 (2017).
22. Shendruk, T. N., Doostmohammadi, A., Thijssen, K. & Yeomans, J. M. Dancing disclinations in confined active nematics. *Soft Matter* **13**, 3853–3862 (2017).
23. Lemma, L. M., DeCamp, S. J., You, Z., Giomi, L. & Dogic, Z. Statistical properties of autonomous flows in 2D active nematics. *Soft Matter* **15**, 3264–3272 (2019).
24. Ramaswamy, S. The mechanics and statistics of active matter. *Annu. Rev. Condens. Matter Phys.* **1**, 323–345 (2010).
25. Marchetti, M. C. et al. Hydrodynamics of soft active matter. *Rev. Mod. Phys.* **85**, 1143–1189 (2013).
26. Aref, H. Stirring by chaotic advection. *J. Fluid Mech.* **143**, 1–21 (1984).
27. Aref, H. et al. Frontiers of chaotic advection. *Rev. Mod. Phys.* **89**, 025007 (2017).
28. Boyland, P. L., Aref, H. & Stremler, M. A. Topological fluid mechanics of stirring. *J. Fluid Mech.* **403**, 277–304 (2000).
29. Muzzio, F. J., Swanson, P. D. & Ottino, J. M. The statistics of stretching and stirring in chaotic flows. *Phys. Fluids A* **3**, 822–834 (1991).
30. Chaiken, J., Chevray, R., Tabor, M., Tan, Q. M. & Stuart, J. T. Experimental study of Lagrangian turbulence in a Stokes flow. *Proc. R. Soc. Lond. A* **408**, 165–174 (1986).
31. Aref, H. & Balachandar, S. Chaotic advection in a Stokes flow. *Phys. Fluids* **29**, 3515–3521 (1986).
32. Vikhansky, A. Chaotic advection of finite-size bodies in a cavity flow. *Phys. Fluids* **15**, 1830–1836 (2003).
33. Gouillart, E., Thiffeault, J.-L. & Finn, M. D. Topological mixing with ghost rods. *Phys. Rev. E* **73**, 036311 (2006).
34. Finn, M. D. & Thiffeault, J.-L. Topological optimization of rod-stirring devices. *SIAM Rev.* **53**, 723–743 (2011).
35. Thiffeault, J.-L. Braids of entangled particle trajectories. *Chaos* **20**, 017516 (2010).
36. Allshouse, M. R. & Thiffeault, J.-L. Detecting coherent structures using braids. *Physica D* **241**, 95–105 (2012).
37. Budišić, M. & Thiffeault, J.-L. Finite-time braiding exponents. *Chaos* **25**, 087407 (2015).
38. Roberts, E., Sindi, S., Smith, S. A. & Mitchell, K. A. Ensemble-based topological entropy calculation (E-tec). *Chaos* **29**, 013124 (2019).

39. Hirokawa, N., Noda, Y., Tanaka, Y. & Niwa, S. Kinesin superfamily motor proteins and intracellular transport. *Nat. Rev. Mol. Cell Biol.* **10**, 682–696 (2009).
40. Lu, W., Winding, M., Lakonishok, M., Wildonger, J. & Gelfand, V. I. Microtubule–microtubule sliding by kinesin-1 is essential for normal cytoplasmic streaming in *Drosophila* oocytes. *Proc. Natl Acad. Sci. USA* **113**, E4995–E5004 (2016).
41. Young, L.-S. in *Entropy* (eds Greven, A., Keller, G. & Warnecke, G.) 313–327 (Princeton Univ. Press, 2003).
42. Visscher, K., Schnitzer, M. J. & Block, S. M. Single kinesin molecules studied with a molecular force clamp. *Nature* **400**, 184–189 (1999).
43. Lam, A. T., Curschellas, C., Krovvidi, D. & Hess, H. Controlling self-assembly of microtubule spools via kinesin motor density. *Soft Matter* **10**, 8731–8736 (2014).
44. Tan, A. J., Chapman, D. E., Hirst, L. S. & Xu, J. Understanding the role of transport velocity in biomotor-powered microtubule spool assembly. *RSC Adv.* **6**, 79143–79146 (2016).
45. Hemingway, E. J., Mishra, P., Marchetti, M. C. & Fielding, S. M. Correlation lengths in hydrodynamic models of active nematics. *Soft Matter* **12**, 7943–7952 (2016).

Acknowledgements

Our group is grateful to Z. Dogic for the generous contribution of microtubules and molecular motors and to L. Lemma for sample preparation. We also acknowledge useful discussions with S. Sindi. The authors acknowledge generous funding from the National Science Foundation, through several awards (DMR-1808926), NSF-CREST: Center for Cellular and Biomolecular Machines at UC Merced (HRD-1547848), and from the Brandeis Biomaterials facility MRSEC-1420382.

Author contributions

L.S.H. and K.A.M. designed the study. A.J.T. carried out the experiments. A.J.T., E.R., S.A.S., U.A.O., J.A., S.F. and K.A.M. performed analysis. L.S.H., K.A.M. and A.J.T. wrote the paper.

Competing interests

The authors declare no competing interests.

Additional information

Supplementary information is available for this paper at https://doi.org/10.1038/s41567-019-0600-y.

Reprints and permissions information is available at www.nature.com/reprints.

Correspondence and requests for materials should be addressed to K.A.M. or L.S.H.

Peer review information: *Nature Physics* thanks Jordi Ignes-Mullol, Idan Tuval and Julia Yeomans for their contribution to the peer review of this work.

Publisher's note: Springer Nature remains neutral with regard to jurisdictional claims in published maps and institutional affiliations.

Methods

Flow-cell preparation. Flow cells for the experiments are constructed from a hydrophilic coverslip and a hydrophobic glass microscope slide as described by Sanchez et al.[15]. This treatment facilitates formation of the oil and water layers necessary for sample preparation. The two surfaces are treated differently so that we can pass oil and water into the flow cell (Supplementary Fig. 6). First, the coverslips are treated with a polyacrylamide brush that allows the surface to be hydrophilic and prevent non-specific binding of proteins[15]. The coverslips are washed with soap and hot water, then rinsed with water three times. The coverslips are submerged in ethanol, rinsed with water, and submerged in 0.1 M NaOH and rinsed with water. Once the coverslips are cleaned, they are placed in a solution containing 98.5% ethanol, 1% acetic acid and 0.5% silane-bonding agent 3-(trimethoxysilyl)propylmethacrylate (Acros Organics) for 15 min. The coverslips are rinsed with water before immersion in an acrylamide solution containing 2% (w/v%) acrylamide, 35 µl per 100 ml of tetramethylethylenediamine (Bio-Rad) and 70 mg per 100 ml of ammonium persulfate. This helps polymerization of the polyacrylamide brush on the surface of the coverslips. The coverslips are stored in this acrylamide gel. Before immediate use, the coverslips are rinsed with water and air-dried. The glass slides are washed with acetone, methanol and ethanol. The slides are then treated with Aquapel to create a hydrophobic surface. About 50 µl of Aquapel glass treatment is dropped onto a glass slide. A second glass slide is placed on top perpendicular to the first slide to spread the solution evenly onto both surfaces and left to sit for 1 min. The slides are then dried with compressed air, rinsed with water and air-dried before use.

Preparation of the 2D active nematic. Microtubule polymerization was carried out and kinesin–streptavidin clusters prepared as previously reported by the Dogic laboratory[15]. Biotin-coated 2-µm-diameter silica beads (Nanocs) are diluted to 5,000 beads µl^{-1} in M2B buffer (80 mM PIPES at pH 6.8, 2 mM $MgCl_2$, 1 mM EGTA) and bath sonicated for 30 min to 1 h to break up bead aggregates. An active premixture containing biotin–kinesin, streptavidin, PEG (poly(ethylene glycol)) and PKLDH (an ATP-regenerating system) is prepared as previously described by Sanchez et al.[15]. Two antioxidant mixtures are used along with Trolox to avoid photobleaching during the imaging. Antioxidant solution AO1 contains 150 mg ml^{-1} glucose and 250 mM dithiothreitol. Antioxidant solution AO2 contains 10 mg ml^{-1} glucose oxidase and 1.75 mg ml^{-1} catalase. The kinesin–streptavidin motor clusters (KSA) are made by combining 0.31 mg ml^{-1} K401 kinesin motors, 0.18 mg ml^{-1} streptavidin and 2.2 µg ml^{-1} dithiothreitol and incubated on ice for 30 min. This mixture is diluted with M2B in the ratio 1:8.6. A high-salt buffer (MIX) is prepared containing 69 mM $MgCl_2$ diluted in M2B. The ATP-regenerating system is prepared with 917 units ml^{-1} pyruvate kinase and 913 units ml^{-1} lactate dehydrogenase in aqueous buffered glycerol solution (PKLDH). The final premixture is produced by adding 1.33 µl AO1, 1.33 µl AO2, 1.7 µl PKLDH, 2.9 µl MIX, 4 µl KSA, 6 µl 20 mM Trolox, 8 µl 200 mM phosphoenolpyruvate and 8 µl 6% (w/v) 20 kD PEG. The premixture is separated into 6.64 µl aliquots. To form the active network, we take one aliquot of the premixture and add ATP (50–1,000 µM) and fill to 10 µl with M2B. Then 2 µl of 6 mg ml^{-1} Alexa-647-labelled GMPCPP microtubules (~3% labelling) is added to 10 µl of the premixture. The mixture is incubated for 5–30 min at room temperature to allow the network to form. The network takes longer to form for lower ATP concentrations. Finally, 0.5 µl of the silica bead solution is added to the microtubule network and gently tapped to mix. A 6 µl volume flow cell is created by first placing strips of double-sided tape about 3 mm apart on a hydrophobic Aquapel-treated glass slide. Then, an acrylamide-coated coverslip is placed on top to create a channel open at both ends (Supplementary Fig. 6). To create the active microtubule layer, we first pass an oil–surfactant mixture (HFE7500 with 1.8% (v/v) PFPE–PEG–PFPE (perfluoropolyether) surfactant) into the channel. Then we immediately exchange the oil–surfactant mixture by introducing the aqueous component containing the active microtubule network including the biotin beads. The flow cell is sealed with ultraviolet-curable glue (RapidFix). To confine the active network into a quasi-2D layer, we place the filled flow cell in a swinging bucket rotor (Sorvall Legend RT+ centrifuge, four-place swinging bucket rotor), and spin the material down for 42 min at 350 r.p.m. This step allows the active fluid to assemble at the oil–water interface inside the flow cell.

PIV analysis. PIV analysis was carried out with the MATLAB PIVlab 1.43 package[46], using the default graphical user interface settings. PIVlab uses sequential images to calculate a velocity vector field for each frame. We analysed both bright-field and fluorescence microscopy videos at every ATP concentration. For each experimental run, v_{rms} was computed in the centre of the velocity frame. We calculated the average velocity vector in each frame and subtracted it from every velocity vector in the frame to obtain the velocity field in the centre of the velocity frame. We then calculated the resulting root-mean-squared velocity for each frame, and averaged over all frames for the final v_{rms} value.

We also used the PIV velocities to compute the velocity–velocity correlation length for each data run, as in refs. [23,45]. The velocity autocorrelation function was computed as $C(r)=\sum_{ij}\hat{\mathbf{v}}_i\cdot\hat{\mathbf{v}}_j\delta(r-r_{ij})$, where the indices i and j range over all frames and all grid points within a frame, $\hat{\mathbf{v}}_i=\mathbf{v}_i/|\mathbf{v}_i|$ is the unit velocity vector and $r_{ij}=|\mathbf{r}_i-\mathbf{r}_j|$, for grid points $\mathbf{r}_i$ and $\mathbf{r}_j$. Numerically, the delta function is approximated as a rectangle. The correlation length was taken to be the distance at which $C(r)$ decayed to half its value at $r=0$.

Imaging and analysis. The active nematic is imaged using a (Leica DMP) fluorescence microscope and a QImaging Retiga Exi camera. Fluorescence microscopy videos are recorded with a 500 ms exposure time per frame and a 100 ms time interval between frames. The bright-field microscopy videos of the beads are recorded using a 10 ms exposure per frame with 100 ms intervals between frames. We used a MATLAB-adapted tracking algorithm to track bead trajectories[47]. The bead attachment was very stable over the timescale of a typical experiment. Any unbound beads were easy to distinguish and eliminate from the analysis due to their characteristic Brownian motion and tendency to sediment to the glass surface when centrifuged. Any bead clusters were also eliminated from the analysis. To measure the separation distance between beads with diverging trajectories, we used the segmented line tool in ImageJ to measure the nematic contour length between beads for each successive frame throughout the video.

Computation of director field and topological defect locations. We wrote MATLAB code to compute the director at each grid point using a windowed Fourier transform. A Gaussian filter was first applied to the image, centred on the selected grid point. The Fourier transform of the filtered image was then applied, followed by a second Gaussian filter on the radius in Fourier space. The covariance matrix of the resulting distribution in Fourier space was then computed, and the director was taken to point along the largest eigenvector.

Topological defects were identified from regions of rapid rotation of the director field. Specifically, we identified isolated patches of grid points in the image domain in which the change in the director was large ($\delta\theta\geq\pi/4$) between neighbouring grid points. The topological charge for each such patch was computed from $\Delta\theta/(2\pi)$, summed along the loop surrounding, but just outside, the patch, thereby guaranteeing that $\delta\theta<\pi/4$ between successive grid points.

Lyapunov exponent from velocity field. We computed the Lyapunov exponent directly from the microtubule velocity field. We used PIV (specifically the MATLAB PIVlab package[46]) to compute the velocity as a function of position and time from the fluorescence microscopy video. A local Lyapunov exponent can then be computed at each point in space and time as the parallel derivative of the parallel component of velocity (parallel with respect to the nematic director) (Supplementary Section 5). Averaging over space and time yields $\lambda_{\nabla v}$. (recent work[17,21,23] has also used the PIV velocity gradient as a system diagnostic to detect vortices using the Okubo–Weiss field $-\det(\nabla\mathbf{v})$). In practice, the PIV analysis produces a more reliable component of velocity in the direction perpendicular to the nematic director than parallel to it. We thus compute $\lambda_{\nabla v}=0.0120\ (\pm0.0006)\ s^{-1}$ as the average of (minus) the perpendicular derivative of the perpendicular component of velocity $\mathbf{v}$. These two averages are equal as long as the system is area preserving (on average).

Reporting Summary. Further information on research design is available in the Nature Research Reporting Summary linked to this article.

Data availability

The data that support the findings of this study are available from the corresponding authors on reasonable request.

Code availability

The MATLAB code for computing nematic director fields and topological defects is available on request from K.A.M. The E-tec code is available in Python from S.A.S. (smiths@mtholyoke.edu) on request.

References

46. Thielicke, W. & Stamhuis, E. J. PIVlab—towards user-friendly, affordable and accurate digital particle image velocimetry in MATLAB. *J. Open Res. Softw.* **2**, e30 (2014).
47. Crocker, J. C. & Grier, D. G. Methods of digital video microscopy for colloidal studies. *J. Colloid Interface Sci.* **179**, 298–310 (1996).

nature research

Corresponding author(s): Linda S Hirst and Kevin A. Mitchell

Last updated by author(s): Feb 13, 2019

Reporting Summary

Nature Research wishes to improve the reproducibility of the work that we publish. This form provides structure for consistency and transparency in reporting. For further information on Nature Research policies, see Authors & Referees and the Editorial Policy Checklist.

Statistics

For all statistical analyses, confirm that the following items are present in the figure legend, table legend, main text, or Methods section.

n/a	Confirmed	
☐	☒	The exact sample size (*n*) for each experimental group/condition, given as a discrete number and unit of measurement
☐	☒	A statement on whether measurements were taken from distinct samples or whether the same sample was measured repeatedly
☒	☐	The statistical test(s) used AND whether they are one- or two-sided *Only common tests should be described solely by name; describe more complex techniques in the Methods section.*
☒	☐	A description of all covariates tested
☐	☒	A description of any assumptions or corrections, such as tests of normality and adjustment for multiple comparisons
☐	☒	A full description of the statistical parameters including central tendency (e.g. means) or other basic estimates (e.g. regression coefficient) AND variation (e.g. standard deviation) or associated estimates of uncertainty (e.g. confidence intervals)
☒	☐	For null hypothesis testing, the test statistic (e.g. *F*, *t*, *r*) with confidence intervals, effect sizes, degrees of freedom and *P* value noted *Give P values as exact values whenever suitable.*
☒	☐	For Bayesian analysis, information on the choice of priors and Markov chain Monte Carlo settings
☒	☐	For hierarchical and complex designs, identification of the appropriate level for tests and full reporting of outcomes
☒	☐	Estimates of effect sizes (e.g. Cohen's *d*, Pearson's *r*), indicating how they were calculated

Our web collection on statistics for biologists contains articles on many of the points above.

Software and code

Policy information about availability of computer code

Data collection	Free open Source software, Fiji was used for data analysis
Data analysis	The E-tec algorithm is available at https://zenodo.org/badge/latestdoi/146612307 . We also used PIVLab and Matlab, which are both publicly available packages. Specific Matlab code written for this project is available upon request from author K. Mitchell.

For manuscripts utilizing custom algorithms or software that are central to the research but not yet described in published literature, software must be made available to editors/reviewers. We strongly encourage code deposition in a community repository (e.g. GitHub). See the Nature Research guidelines for submitting code & software for further information.

Data

Policy information about availability of data

All manuscripts must include a data availability statement. This statement should provide the following information, where applicable:

- Accession codes, unique identifiers, or web links for publicly available datasets
- A list of figures that have associated raw data
- A description of any restrictions on data availability

The data that support the findings of this study are available from the corresponding authors upon reasonable request.

Field-specific reporting

Please select the one below that is the best fit for your research. If you are not sure, read the appropriate sections before making your selection.

☒ Life sciences ☐ Behavioural & social sciences ☐ Ecological, evolutionary & environmental sciences

Life sciences study design

All studies must disclose on these points even when the disclosure is negative.

Sample size	For bead pair stretching n varied between 5 and 10 (See Supplementary figure 1) For defect stretching n varied between 10 and 11 (see Supplementary figure 2) where every measurement is recorded for different ATP values. Comparing these results to the standard deviation we determined that the number of data points was sufficient (s.d. also show in SI Figs 1 and2).
Data exclusions	All bead separations and defect separations collected for each active nematic sample are included in the paper and detailed in the SI.
Replication	The measurements of topological entropy as calculated from bead stretching and defect stretching were very reproduceable (See SI Figs 1 and 2) with minimal outliers.
Randomization	This is not relevant to our study. The active matter systems were prepared in the lab for study under different experimental conditions and directly studied using our experimental and computational techniques. No allocation of groups is used.
Blinding	This is not relevant to our work since there are no experimental groups.

Reporting for specific materials, systems and methods

We require information from authors about some types of materials, experimental systems and methods used in many studies. Here, indicate whether each material, system or method listed is relevant to your study. If you are not sure if a list item applies to your research, read the appropriate section before selecting a response.

Materials & experimental systems

n/a	Involved in the study
☒	☐ Antibodies
☒	☐ Eukaryotic cell lines
☒	☐ Palaeontology
☒	☐ Animals and other organisms
☒	☐ Human research participants
☒	☐ Clinical data

Methods

n/a	Involved in the study
☒	☐ ChIP-seq
☒	☐ Flow cytometry
☒	☐ MRI-based neuroimaging